PHYSICAL REVIEW FLUIDS **2**, 094007 (2017)

Controlled liquid entrapment over patterned sidewalls in confined geometries

Ankur Gupta, Hyundo Lee, and Patrick S. Doyle[*]
Massachusetts Institute of Technology, Cambridge, Massachusetts 02139, USA

(Received 8 May 2017; published 28 September 2017)

Liquid entrapment over patterned surfaces has applications in diagnostics, oil recovery, and printing processes. Here we study the process of oil displacement upon sequential injection of water over a photopatterned structure in a confined geometry. By varying the amplitude and frequency of triangular and sinusoidal patterns, we are able to completely remove oil or trap oil in varying amounts. We present a theoretical model based on geometrical arguments that successfully predicts the criterion for liquid entrapment and provides insights into the parameters that govern the physical process.

DOI: 10.1103/PhysRevFluids.2.094007

I. INTRODUCTION

In oil recovery and soil remediation, displacement of liquids such as oils and liquid pollutants from the pores is typically achieved by injecting another liquid [1–6]. The geometric morphology of the pores naturally plays an important role in liquid recovery where surface roughness creates challenges in displacing the trapped liquid. Roughness often plays a detrimental role for the above applications. In contrast, several applications prefer a liquid layer over a rough surface. In diagnostic research, for instance, there is an increasing interest in building microfluidic platforms that create isolated aqueous microreactors. Such isolation of aqueous environment is achieved by introducing an artificial defect on the surface such as an obstacle or a depression [7–11]. Similarly, extensive research on liquid-infused surfaces demonstrates that a trapped liquid layer over a patterned surface lends remarkable surface properties [12–19]. Thus depending on the application, it may be desirable to either remove or trap a liquid layer over a surface.

There have been a series of studies on liquid-infused surfaces with geometric features on the order $\sim 10\ \mu\text{m}$ where the authors show how the preexisting layer of oil in a groove (a model for a liquid-infused surface) can be drained by injecting water [16–19]. They also examined the effect of aspect ratio of the groove, presence of obstacles, viscosity ratio of the two phases, and presence of surfactant in the aqueous phase on the oil drainage. Though these studies are very useful for fundamental understanding of the oil drainage process, the investigators did not consider the effect of groove shape. Recently, we studied oil entrapment over isolated obstacles and demonstrated the importance of obstacle shape in controlling the entrapment process [20].

In this article, we systematically examine the displacement of a preexisting layer of oil over a photopatterned wavy surface to understand the effect of surface roughness on displacement of oil. Specifically, we study the effect of oil displacement by water over triangular- and sinusoidal-patterned sidewalls in a microchannel. The variations in amplitude and frequency allow us to control the surface roughness. We describe a simple geometrical model to explain the evolution of the interface and validate it with our experimental results. The model provides useful physical insights about the process and specifically helps identify relative importance of dimensionless length scales that govern the system. We experimentally validate the criterion to remove or trap the preexisting oil inside the pattern. We believe our results will be useful for research in oil recovery, soil remediation, diagnostics, and liquid-infused surfaces. Our study can also be useful in fiber coating and printing applications where the shape of fibers and printing grooves can influence the physical process [21–25]. Last, we hope our results will help researchers building models for porous media flows to incorporate the effect of surface shape.

---

[*] pdoyle@mit.edu

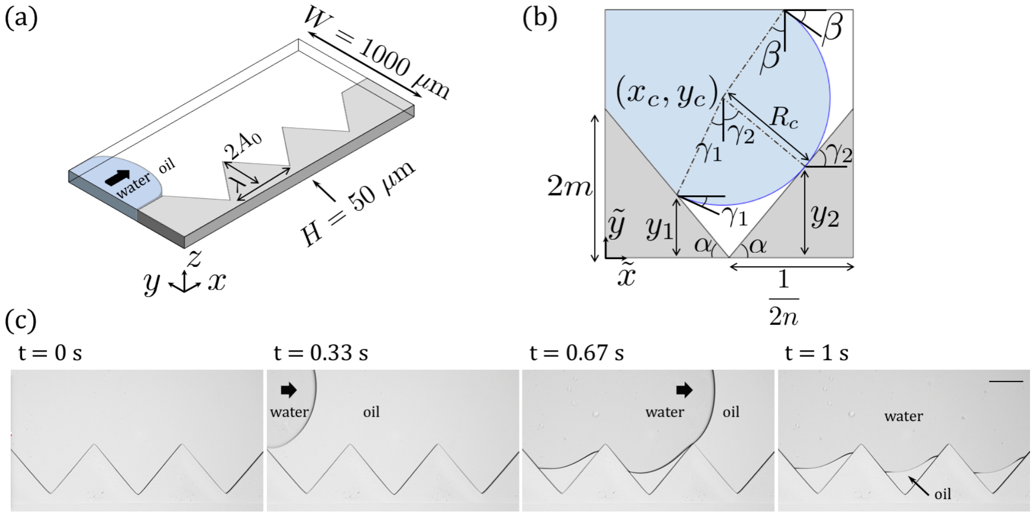

FIG. 1. (a) Schematic of the experimental setup. Immiscible liquid-liquid displacement in a glass microchannel over a triangular-patterned sidewall. The channel is first filled with oil (decane), and then water is introduced into the channel. (b) Schematic of the theoretical setup. The triangular geometry can be represented by two dimensionless length scales: amplitude $m = \frac{A_0}{W}$ and frequency $n = \frac{W}{\lambda}$. We also define angle α such that $\tan(\alpha) = 4mn$. For low capillary and Reynolds numbers, we approximate the interface between oil and water as a circular arc that satisfies static contact angle conditions at fluid-solid interfaces. We describe the circular arc in terms of angle of intersection with horizontal at left-triangular wall (γ_1), angle of intersection with horizontal at right-triangular wall (γ_2), and angle of intersection with horizontal at top sidewall (β). (c) Time-series microscope images from experiments during the immiscible displacement process. Scale bar is 200 μm.

We present our experimental and theoretical setup in Sec. II where we introduce the dimensionless groups that govern the process. In Sec. III we provide results and discussion where we emphasize the geometric relations that lead to complete displacement, partial displacement, and complete entrapment of oil within the patterned structures. We also show that our experimental and theoretical results are in good agreement. Finally, we discuss the implication of our results for practical applications and future research in Sec. IV.

II. EXPERIMENTAL AND THEORETICAL SETUP

A schematic of our experimental setup to study immiscible liquid displacement is presented in Fig. 1(a). We use an acrylated glass microchannel (Hilgenberg GmbH) with length $L = 18$ mm (x direction), width $W = 1$ mm (y direction), and height $H = 50$ μm (z direction). We first fill the channel with a mixture of photocurable polyurethane acrylate precursor (MINS 311RM, Minuta Tech.) with 5% (volume/volume) photoinitiator 2-hydroxy-2-methylpropiophenone (Sigma-Aldrich). Using microscope-projection lithography, we photopattern a repetitive structure at one of the sidewalls [11,20,26–30]. In this study, we pattern triangular and sinusoidal structures with 30 different combinations of wavelength (λ) and amplitude (A_0). We use six different wavelengths $\lambda = [250, 350, 400, 500, 750, 1000]$ μm and five different amplitudes $2A_0 = [75, 100, 200, 300, 400]$ μm. For a distance of 250 μm before and after the pattern, we create a flat structure with amplitude $2A_0$ to ensure smooth displacement at the entrance and exit. After the photopatterning step, we sequentially fill the channel with oil (decane, Sigma-Aldrich) and water by a syringe pump (Harvard Apparatus) at a constant flow rate $Q = 5$ μl/min.

To model our physical system, we define the following variables: density of water ρ_w (10^3 kg/m^3), density of oil ρ_o (760 kg/m^3), viscosity of water μ_w (1 mPa s), viscosity of oil μ_o (1 mPa s), interfacial tension between oil and water σ (52 mN/m), oil-in-water contact angle with patterned sidewall θ, and oil-in-water contact angle with unmodified sidewall β. Physical variables combined with geometrical parameters yield several dimensionless groups such as Reynolds number $\mathrm{Re} = \frac{\rho_w Q}{W\mu_w}$, capillary number $\mathrm{Ca} = \frac{\mu_w Q}{WH\sigma}$, aspect ratio $\frac{H}{W}$, dimensionless amplitude $m = \frac{A_0}{W}$, dimensionless frequency $n = \frac{W}{\lambda}$, viscosity ratio $N = \frac{\mu_o}{\mu_w}$, and contact angles θ and β. We also define angle α such that $\tan(\alpha) = 4mn$.

As we demonstrated in our previous work, significant simplifications are possible under certain physical conditions for an immiscible liquid displacement process [20]. We can neglect effects due to viscosity contrast since we use decane and water in our system for which $N \approx 1$. For the operating conditions we used in our system, $\mathrm{Re} \approx 0.08$ and $\mathrm{Ca} \approx 3 \times 10^{-5}$. Low values of Re and Ca imply that interfacial stress significantly dominates over viscous and inertial stresses, and so the interface is not perturbed by the flow. Therefore, we neglect the pressure drop over a length scale of W within the water phase $\Delta P \sim \frac{12\mu_w Q}{H^3}$ relative to pressure drop across the interface $\Pi \sim 4\sigma(\frac{1}{W} + \frac{1}{H})$ as $\frac{\Delta P}{\Pi} \approx 3\mathrm{Ca}(\frac{W}{H}) \approx 6 \times 10^{-4}$. A similar analysis is also possible for the oil phase. Therefore we assume quasistatic flow conditions and model the interface between oil and water phase in the x–y plane as a circular arc that satisfies the static contact angle conditions at the fluid-solid boundaries. We discuss the effect of variations in Ca and N in Sec. III.

Figure 1(b) is a schematic of our theoretical setup for a triangular-patterned sidewall. We assume the origin to be at the bottom left corner and scale the coordinates with W to define $\tilde{x} = \frac{x}{W}$ and $\tilde{y} = \frac{y}{W}$. In rest of the article, all the discussion is in a dimensionless coordinate system, and for simplicity, we drop the tilde from the dimensionless coordinates. To construct a circular arc, we need to find three quantities: x coordinate of the center of the arc x_c, y coordinate of the center of the arc y_c, and the radius of the arc R_c. In particular, we are interested in the arc that subtends an angle γ_1 with horizontal at the left triangular wall, γ_2 with horizontal at the right triangular wall, and β with horizontal at the top sidewall. We note that the height of the intersection at left and right triangular walls needs to be such that $0 \leqslant y_1, y_2 \leqslant 2m$. Though it might appear that the arc should always intersect the left triangular wall at angle θ or $\gamma_1 = \alpha - \theta$, and should touch the right triangular wall or $\gamma_2 = \alpha$, we show later that since y_1 and y_2 are bounded, γ_1 and γ_2 are not always α-θ and α, respectively.

Figure 1(c) shows representative time series of microscope images during the immiscible displacement process. As the water displaces the oil phase in a triangular trough, the interface moves downward on the left triangular wall until the interface touches the right triangular wall (see $t = 0.67$ s). The interface then pinches off and breaks into two parts where one part stays behind with the trapped oil and the other progresses to the next triangular trough. The microscope images suggest that after the breakup of the interface, the interface with the trapped oil readjusts its curvature to satisfy the contact angle condition. For a case with no contact angle hysteresis, we would expect a symmetrical oil entrapment post-pinch-off. However, our system shows an asymmetrical interface post-pinch-off (see $t = 1$ s) suggesting that there is an effect of contact angle hysteresis. We discuss the effect of contact angle hysteresis in the Appendix. We note that our geometrical model is a first-order approximation of the actual experiments and captures only the interface evolution until the interface meets the right triangular wall. Also, as mentioned before, we do not predict evolution of interface with time and compare only quasistatic interface shapes.

We now discuss how to evaluate x_c, y_c, and R_c. From Fig. 1(b), we write the following equations using geometry:

$$y_c = y_1 + R_c \cos\gamma_1, \tag{1}$$

$$y_c = y_2 + R_c \cos\gamma_2, \tag{2}$$

$$1 = y_c + R_c \cos\beta, \tag{3}$$

$$x_c = \frac{1}{2n} - \frac{y_1}{\tan\alpha} + R_c \sin\gamma_1, \tag{4}$$

$$x_c = \frac{1}{2n} + \frac{y_2}{\tan\alpha} - R_c \sin\gamma_2. \tag{5}$$

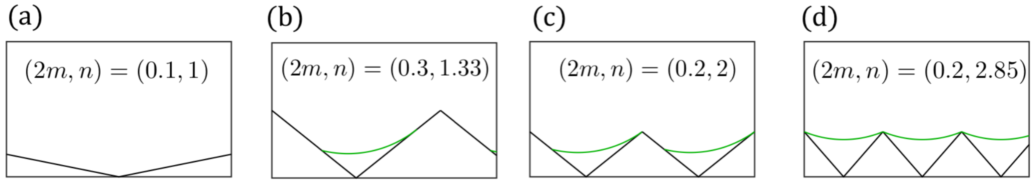

FIG. 2. Four representative cases for oil capture in a triangular pattern obtained from theory: (a) $y_1 = 0$, $y_2 = 0$, (b) $0 < y_1 < 2m, 0 < y_2 < 2m$, (c) $0 < y_1 < 2m, y_2 = 2m$, and (d) $y_1 = 2m, y_2 = 2m$.

Equations (1)–(5) are also subjected to the constraints $0 \leqslant y_1 \leqslant 2m$ and $0 \leqslant y_2 \leqslant 2m$. Therefore, we divide the entrapment process for a triangular pattern into four cases, as shown in Fig. 2:

(1) $y_1 = 0, y_2 = 0$. This is the case of no entrapment, as shown in Fig. 2(a). Here $\gamma_1 = \alpha - \theta$ and $\gamma_2 = \alpha$. We subtract Eq. (4) from Eq. (5) to obtain $y_1 + y_2 = R_c \tan\alpha[\sin\alpha + \sin(\alpha - \theta)]$. Upon simplification we obtain $y_1 + y_2 \leqslant 0$ when

$$\tan\alpha = 4mn \leqslant \tan\frac{\theta}{2}. \tag{6}$$

Hence, there is no capture when $4mn \leqslant \tan\frac{\theta}{2}$. This is consistent with qualitative expectation, i.e., for higher values of m and n, or larger amplitudes and frequencies, we are more likely to get oil entrapment.

(2) $0 < y_1 < 2m, 0 < y_2 < 2m$. This is the case of entrapment when both y_1 and y_2 are not at the end of left and right triangular walls, as shown in Fig. 2(b). As discussed, for this case, we require that $4mn > \tan\frac{\theta}{2}$. In this case too, $\gamma_1 = \alpha - \theta$ and $\gamma_2 = \alpha$. Therefore, we solve Eqs. (1)–(5) to get x_c, y_c, R_c, y_1, and y_2. Here we give the solutions of y_1 and y_2 after simplifications [the rest of the variables can be evaluated from Eqs. (1)–(5)]:

$$y_2 = \frac{\cos^2\frac{\theta}{2} - \cos^2\alpha}{\cos^2\frac{\theta}{2} + \cos\alpha\cos\beta}, \tag{7}$$

$$y_1 = y_2\left(\frac{1 - \frac{\tan\frac{\theta}{2}}{\tan\alpha}}{1 + \frac{\tan\frac{\theta}{2}}{\tan\alpha}}\right). \tag{8}$$

Equations (7)–(8) show that $y_1 \leqslant y_2$. Since above equations are valid only when $0 \leqslant y_2 \leqslant 2m$, we can also evaluate the condition for α when $y_2 = 2m$ from Eq. (7) (not discussed here). Moreover, we also recover Eq. (6), i.e., $y_1, y_2 = 0$ when $\tan\alpha = \tan\frac{\theta}{2}$.

(3) $0 < y_1 < 2m, y_2 = 2m$. This is the case of entrapment when y_2 is at the end of right triangular wall but y_1 is still in the middle, as shown in Fig. 2(c). In such a case, the interface intersects the right triangular wall at an angle and is no longer tangential. We solve for $x_c, y_c, R_c, y_1, \gamma_2$ from Eqs. (1)–(5) by substituting $y_2 = 2m$, $\gamma_1 = \alpha - \theta$, and keeping γ_2 as a variable. Below we provide a solution for γ_2 after appropriately rearranging the equations [the rest of the variables can be calculated from Eqs. (1)–(5)]:

$$\cos\gamma_2 + \left(\frac{4m}{2m+1}\right)\cos\beta + \left(\frac{2m-1}{2m+1}\right)\frac{\cos\theta}{\cos\alpha} + \left(\frac{2m-1}{2m+1}\right)\tan\alpha\sin\gamma_2 = 0. \tag{9}$$

Equation (9) has an analytical solution for $\cos\gamma_2 = \frac{-c_1 + \sqrt{b_1^4 + b_1^2(1-c_1^2)}}{1+b_1^2}$ where $b_1 = (\frac{2m-1}{2m+1})\tan\alpha$, $c_1 = (\frac{4m}{2m+1})\cos\beta + (\frac{2m-1}{2m+1})\frac{\cos\theta}{\cos\alpha}$. Thus we can evaluate the complete solution for the case when the interface reaches top of the right triangular wall.

(4) $y_1 = 2m$, $y_2 = 2m$. This is the case of entrapment when both y_1 and y_2 are at the end of left and right triangular walls, as shown in Fig. 2(d). We solve Eqs. (1)–(5) by using $y_1 = 2m$, $y_2 = 2m$ and substituting γ_1 and γ_2 as variables. We observe that the system is now symmetric or

$\gamma_1 = \gamma_2 = \gamma$. Here we provide an equation to solve for γ [the rest of the variables can be calculated from Eqs. (1)–(5)]:

$$\cos\gamma + \cos\beta + \tan\alpha\left(\frac{2m-1}{2m}\right)\sin\gamma = 0. \tag{10}$$

Equation (10) also has an analytical solution for $\cos\gamma = \frac{-c_1+\sqrt{b_1^4+b_1^2(1-c_1^2)}}{1+b_1^2}$ where $b_1 = (\frac{2m-1}{2m})\tan\alpha$, $c_1 = \cos\beta$. Equation (10) is independent of θ, which is expected since the interface at the left triangular wall is not subtending the contact angle. Also, for the extreme case of $\alpha = \pi/2$, the equation yields $\gamma = 0$, or the interface becomes a straight line connecting the extreme points of the triangular pattern. This result is also consistent with expectation. Last, the condition for $y_1 = 2m$ also captures the effect of pinning, i.e., for large values of $\tan\alpha$ or larger slopes of triangular pattern, the interface is pinned at the extreme point at the left triangular wall and traps a large amount of oil.

Once the values of y_1 and y_2 are calculated, we also find the amount of oil trapped by calculating the area between the interface and the patterned surface (see the Appendix for the full solution). However, we can approximate the amount of oil trapped by finding the area of triangle formed by y_1, y_2 and the lowest point of the trough. The dimensionless amount of oil entrapped $\tilde{a}$ is defined as the ratio of the area between the interface and the pattern relative to the area of the pattern:

$$\tilde{a} \approx \frac{\frac{1}{2}\frac{y_1}{\sin\alpha}\frac{y_2}{\sin\alpha}\sin(\pi-2\alpha)}{\frac{4m^2}{\tan\alpha}} \approx \frac{y_1 y_2}{4m^2}. \tag{11}$$

For a constant value of mn (or α) and θ, Eq. (11) predicts the following:

$$y_1 = 0, \quad y_2 = 0 \Rightarrow \tilde{a} = 0, \tag{12}$$

$$y_1 < 2m, \quad y_2 < 2m \Rightarrow \tilde{a} \sim m^{-2}, \tag{13}$$

$$y_1 < 2m, \quad y_2 = 2m \Rightarrow \tilde{a} \sim m^{-1}, \tag{14}$$

$$y_1 = 2m, \quad y_2 = 2m \Rightarrow \tilde{a} \sim 1. \tag{15}$$

III. RESULTS AND DISCUSSIONS

A summary of our experimental and theoretical results for a range of m and n is provided in Fig. 3. Values of $\theta = \frac{25\pi}{180}$ and $\beta = \frac{35\pi}{180}$ are used for theoretical calculations (see the Appendix for experimental basis of values for θ and β). Overall our experimental and theoretical results are consistent with expectation since the amount of trapped oil increases with increase in both m and n. A qualitative comparison between amount of oil trapped in images from experiments and predicted from theory suggests good agreement. We note that the higher the value of m, the critical value of n at which there is nonzero oil capture is lower. We predict this trend in Eq. (6) that for a nonzero oil capture the frequency should be greater than $n_{\text{crit, theory}} = \frac{1}{4m}\tan(\frac{\theta}{2})$. For $2m = [0.075, 0.1, 0.2, 0.3, 0.4]$, our model predicts $n_{\text{crit, theory}} = [2.7, 2.0, 1.0, 0.59, 0.51]$. The experiments show nonzero capture for $n \geqslant [2.8, 2.5, 1.33, 1.0, 1.0]$, which is in accordance with our prediction.

Equation (6) shows we can combine the effect of amplitude and frequency to predict the transition from no capture to capture in the parameter mn, a measure of slope of the triangle. Since the slope stays constant in a triangular pattern, we photopolymerized a sinusoidal structure with the equation $y = m[1 + \cos(2\pi nx)]$ to explore the effect of variation in local slope. We created structures with the same ranges of m and n to do a direct comparison with the results from the triangular patterns. We also modified the theoretical calculations for sinusoidal patterns (see the Appendix for details).

The results from sinusoidal patterns are summarized in Fig. 4. Figure 4 shows that similar to triangular structures, the oil capture increases with m and n, and experimental trends are captured by the theory. For $2m = [0.075, 0.1, 0.2, 0.3, 0.4]$, we observe that the experiments show nonzero capture in a sinusoidal pattern for $n \geqslant [2.5, 2.0, 1.33, 1.0, 1.0]$ and the theory predicts $n_{\text{crit, theory}} =$

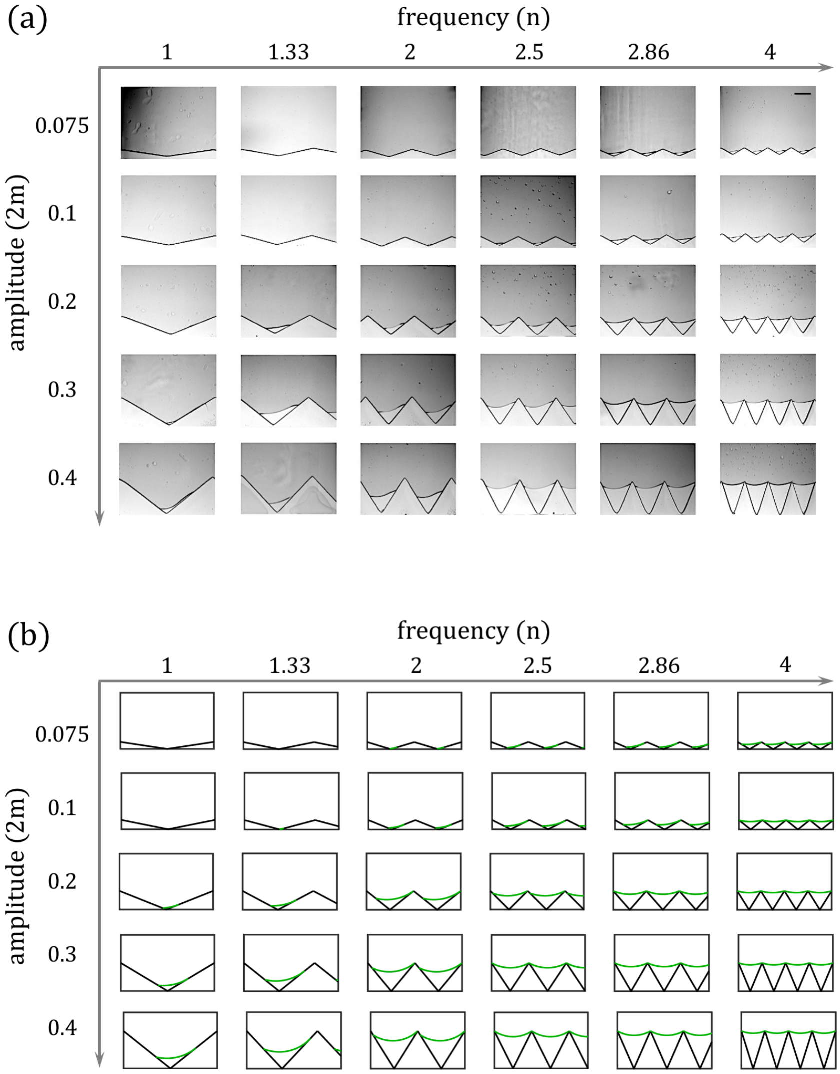

FIG. 3. (a) Experiment results and (b) theoretical map of entrapped oil for triangular pattern with different values of frequency (n) and amplitude ($2m$). The amount of oil trapped increases with increase in amplitude and frequency. Scale bar in experimental images is 200 μm. Values of $\theta = \frac{25\pi}{180}$ and $\beta = \frac{35\pi}{180}$ were used for theoretical calculations.

[2.3,1.9,1.2,0.95,0.8] (see the Appendix for details). Thus experiments and theory are in agreement for the transition from no capture to capture. However, we note that for a sinusoidal pattern, the relationship $n_{\text{crit, theory}} \sim m^{-1}$ is no longer valid since the local slope continuously changes with position. Therefore, a comparison of $n_{\text{crit, theory}}$ between triangular and sinusoidal patterns shows that at low values of m, $n_{\text{theory, crit}}$ is lower for sinusoidal patterns, and the trend reverses for higher values of m. To understand these results, we can envision sinusoidal pattern as piecewise linear segments with varying slopes. At low values of m, the interface is less curved due to lack of confinement. As the interface moves down the left sidewall of the sinusoidal pattern, it meets with regions of large local slope in right side of the pattern, otherwise not possible in a triangular pattern. In contrast, at high values of m, the interface is forced to bend more and misses the region of large local slope. The above result might appear to be counterintuitive since it suggests that for higher values of m,

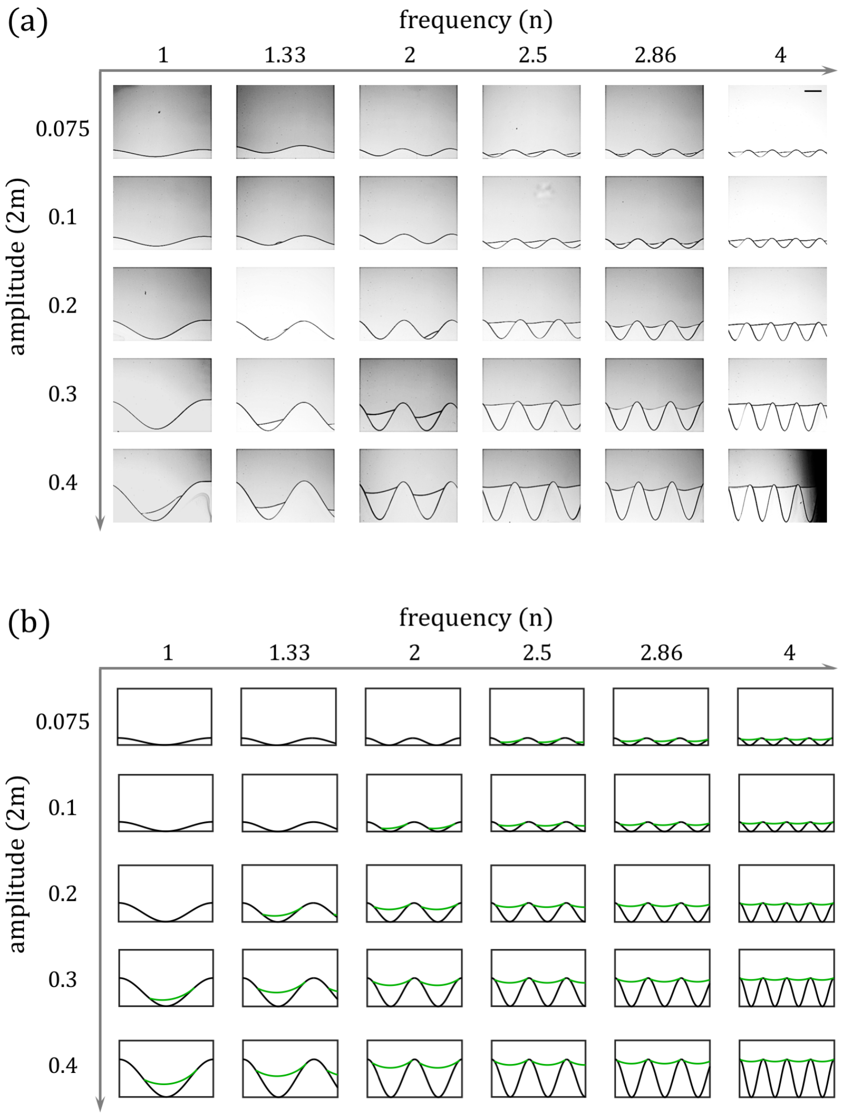

FIG. 4. (a) Experiment and (b) theoretical results of entrapped oil for a sinusoidal pattern with different values of frequency (n) and amplitude ($2m$). The amount of oil trapped increases with increasing amplitude and frequency. Scale bar in experimental images is 200 μm. Values of $\theta = \frac{25\pi}{180}$ and $\beta = \frac{35\pi}{180}$ were used for theoretical calculations.

a sinusoidal pattern needs larger frequencies to trap oil. However, the transition from no capture to capture is not a complete metric to compare the entrapment from the two patterns. We thus compare in Fig. 5 results from experiment and theoretical calculations of dimensionless amount of oil entrapped $\tilde{a}$ for different values of m and n.

Figure 5(a) summarizes results of $\tilde{a}$ for triangular patterns. The theoretical predictions can be understood from the analysis discussed in Eqs. (12)–(15). $\tilde{a}$ has four regimes when plotted with $\tan\alpha = 4mn$, i.e., $\tilde{a} \sim 0$, $\tilde{a} \sim m^{-2}$, $\tilde{a} \sim m^{-1}$, and $\tilde{a} \sim 1$. Therefore, once $\tilde{a} > 0$, the amount of oil entrapped is different for different values of m. However, as $4mn$ increases, the difference between different profiles decrease as all of them approach $\tilde{a} \sim 1$. The experimental data qualitatively agree

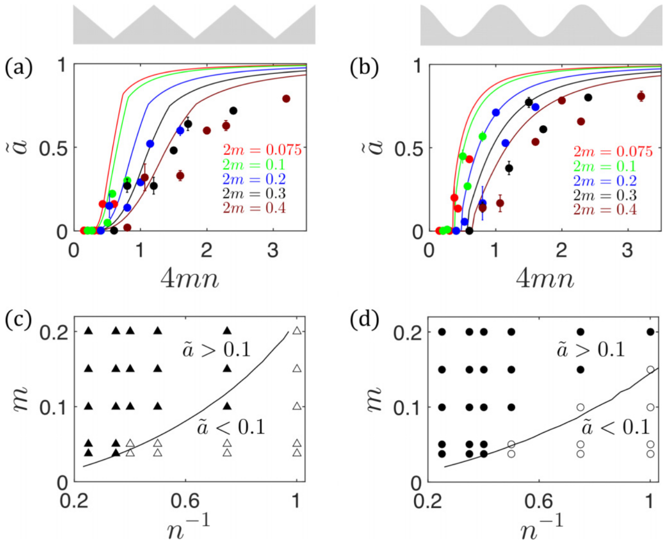

FIG. 5. Dimensionless amount of oil entrapped for (a) triangular pattern and (b) sinusoidal pattern. The symbols represent experimental data and solid lines represent theoretical calculations. Phase diagram of transition from $\tilde{a} < 0.1$ to $\tilde{a} > 0.1$ for (c) triangular pattern and (d) sinusoidal pattern. Closed symbols represent $\tilde{a} > 0.1$, and open symbols represent $\tilde{a} < 0.1$. The solid line is constructed from numerical calculations.

with our theoretical predictions. Nonetheless there are some quantitative differences for several possible reasons. We ignore the effect of the third dimension, which plays a role in the shape of interface. As we show in the Appendix, the contact angle observed from the microscope images is dependent on the position inside the triangular pattern, probably because of the curvature effects in the third dimension [31,32]. However, such effects have been currently ignored in the model since we assume θ to be independent of the third dimension. We also assume the system to be quasistatic and ignore the effect of contact angle hysteresis that might alter the evolution of the interface. For instance, in Fig. 1(c), during the pinch-off process, the interface readjusts near the point of contact ($t = 0.67s$). We do not account for any preferred values of γ_2 based on surface energies in our model. Last, a thin layer of oil that may be deposited in the photopatterned structure can alter the contact angle and surface properties of the structure [20].

Figure 5(b) summarizes results of $\tilde{a}$ for the sinusoidal patterns. There are some similarities and some differences when compared to the triangular pattern. Like the triangular pattern, theoretical profiles $\tilde{a}$ are 0 for low values of $4mn$ (a measure of average slope), but the curves for different values of m do not become nonzero at the same value of $4mn$. This is expected since $n_{\text{crit, theory}} \sim m^{-1}$ doesn't hold for a sinusoidal pattern, as previously discussed. Similar to triangular patterns, for moderate values of $4mn$, different m values yield different $\tilde{a}$ profiles, and for high values of $4mn$ all curves start to approach a limiting value. The experimental data also agree qualitatively with the theoretical predictions. However, a major difference in the predicted profiles of the two patterns is that once $\tilde{a} > 0$, sinusoidal patterns display a steep rise in $\tilde{a}$ whereas triangular patterns show a rather gradual rise in $\tilde{a}$. This happens because once the critical condition is reached, the entrapment is significant due to a concave shape in the middle portion of the sinusoidal pattern. This is visually supported upon comparing Figs. 3 and 4 where entrapment is larger for the sinusoidal pattern. This result underscores the need to include the effect of pattern shape to predict the process of entrapment. Moreover, it also shows that looking at the transition from no capture to capture doesn't provide a complete picture.

Figures 5(c) and 5(d) show the transition from $\tilde{a} < 0.1$ to $\tilde{a} > 0.1$ for both the patterns. The solid lines in phase diagrams show the minimum value of m for a given n at which the $\tilde{a} = 0.1$. We note

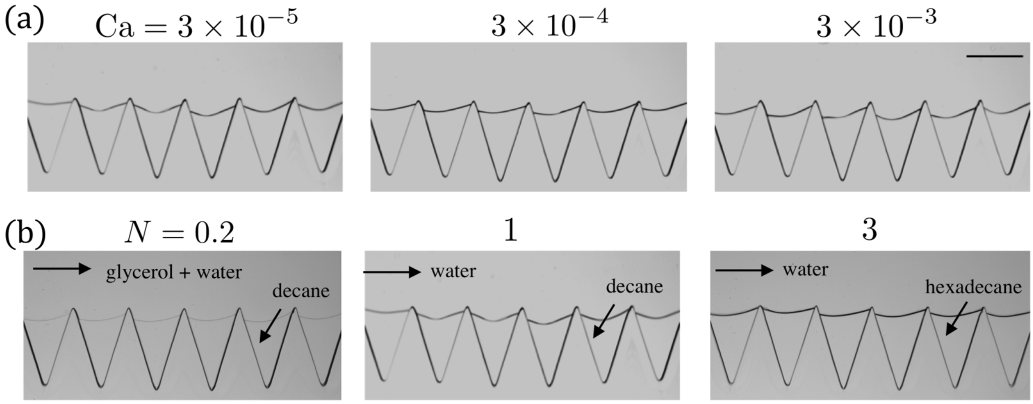

FIG. 6. Effect of capillary number Ca and viscosity ratio N on liquid entrapment. (a) We vary Ca by two orders of magnitude by increasing the flow rate of the flooding phase. We do not observe any significant variation in entrapped oil. Decane is used as trapped phase, and water is used as flooding phase ($N = 1$). (b) We obtain $N = 0.2$ by using mixture of water + glycerol (viscosity = 5 mPa s) as a flooding phase with decane as entrapped phase. Similarly, we obtain $N = 3$ by using water as flooding phase and hexadecane (viscosity = 3 mPa s) as trapped phase. We do not observe any significant variation on entrapment with N. Ca $\sim 10^{-5}$. Scale bar is 200 μm, $2m = 0.4$,$n = 4$.

that the sinusoidal patterns are able to trap $\tilde{a} = 0.1$ at smaller values of m as compared to triangular patterns. This is consistent with analysis from Figs. 5(a) and 5(b). Moreover, the value of $a = 0.1$ is just an example, and similar phase diagrams can be constructed for other values of $\tilde{a}$. Overall the results from experiments agree with predicted phase diagram.

Our analysis suggests some useful design principles. For applications where one wants to trap a large amount of oil, higher values of mn, lower values of m, and large variations in local slope would be preferred. Though $mn \geqslant \frac{1}{4} \tan \frac{\theta}{2}$ is derived for a triangular pattern, it may be a good starting point to estimate the overall global slope. Similarly, depending on the desired value of $\tilde{a}$, different values of m can be used. For instance in applications where width is not defined, dynamic length scales controlled by process parameters can provide flexibility to tune the value of m. On the other hand, if we wish to first deposit and then remove a layer of liquid from a patterned surface, the pattern should have lower values of mn, higher values of m, and small variations in local slope.

We note that our analysis is currently limited to a structure that is periodic in only one direction. However, there are several geometrical systems that are periodic in two directions [12–19]. The challenge in extending our approach to such systems arises from the effect of wetting dynamics since the interface can now progress in two directions and interface speed is required to predict relative movement between the two directions. We refer the readers to reports that discuss these effects [33,34]. We also note that our analysis is currently restricted to a case where liquid flows parallel to the corrugated surface, and the results would be modified if the flow direction changes. However, our current approach of circular arc approximation can still be extended to a different flow direction.

To understand the validity of our model, we vary both capillary number Ca and viscosity ratio N. The results are summarized in Fig. 6. We vary Ca by increasing the water flow rate Q = 5–500 μl/min and observe that liquid entrapment remains unaffected upon increase in Ca by two orders of magnitude [Fig. 6(a)]. This is consistent with expectation since Ca $\sim O(10^{-1})$ is required for droplet breakup in unbounded flows [35]. Even in confined flows, large deformations in droplets are estimated to occur beyond Ca $\sim O(10^{-2})$ [36]. Therefore, we expect our circular arc approximation to hold until Ca $\sim O(10^{-2})$. We also vary N by modifying the flooding and trapped phases [Fig. 6(b)]. Water as flooding phase and decane as trapped phase gives $N = 1$. By using a mixture 50 w% water–50 w% glycerol (viscosity = 5 mPa s) as flooding phase and decane as trapped phase, we get $N = 0.2$. Last, by using water as flooding phase and hexadecane (viscosity $= 3\,\mathrm{mPa\,s}$) as trapped phase, we get $N = 3$. In these experiments, we keep the minimum flow rate of $Q = 5\ \mu\mathrm{l/min}$. The results clearly show that N doesn't affect the entrapment process significantly. We note that this is also consistent with expectation since deformation of an interface is similar for $N \sim O(1)$ in both confined and unconfined flows [35,36]. Therefore our model is valid until $\mathrm{Ca} < O(10^{-2})$ and $N \sim O(1)$.

IV. CONCLUSION

In this article, we discussed the process of liquid entrapment by sequential injection of immiscible liquids. We experimentally photopatterned triangular and sinusoidal structures with different dimensionless amplitudes m and dimensionless frequencies n, and built a quasistatic model that predicts the process of entrapment by approximating the interface as a circular arc. Our experimental and theoretical results are in good agreement, and our analysis highlights the importance of including the shape of the pattern in understanding the entrapment process. Specifically, we discuss using global slope mn, dimensionless amplitude m, and shape of pattern as design principles to control the entrapment process.

We believe our work can be useful for several applications. In oil recovery and soil remediation research, our platform can be used to quantitatively investigate the effect of shape of surface on enhanced oil recovery, and to rapidly screen chemicals that are successful in removing a trapped layer of oil. The effect of wetting in oil recovery can also be explored by combining experimental and theoretical research. Researchers interested in parallel experimentation for diagnostic research may also find this platform useful for creating several isolated aqueous pockets. Moreover, our platform can be easily adapted for large-scale phtopatterning and advanced microscopy techniques that allow this platform to be used for existing material synthesis methods [37]. For applications in designing liquid-infused surfaces, our results could provide design principles for successful entrapment of liquid layers. Understanding the effect of surface shape and amplitude of pattern on entrapment can also help research in the areas of fiber coating and gravure printing processes where dynamic length scales are involved [23–25]. Last, we hope that our results will help researchers building models for porous media flows using first principles to include the surface shape in their models [38,39].

ACKNOWLEDGMENTS

A.G. would like to acknowledge the funding support from the Hugh Hampton Young Fellowship. H.L. would like to acknowledge the funding support from the Samsung Fellowship. P.S.D. acknowledges funding from an MIT Robert T. Haslam Chair. A.G. would like to thank Rohit Kannan for his valuable inputs in theoretical development of the problem.

A.G. and H.L. contributed equally to this work.

APPENDIX

1. Theoretical setup for sinusoidal pattern

A schematic of the theoretical setup for a sinusoidal pattern is provide in Fig. 7. Similar to the triangular pattern, we write the following equations from geometrical balances:

$$y_c = y_1 + R_c \cos \gamma_1, \tag{A1}$$

$$y_c = y_2 + R_c \cos \gamma_2, \tag{A2}$$

$$1 = y_c + R_c \cos \beta, \tag{A3}$$

$$x_c = x_1 + R_c \sin \gamma_1, \tag{A4}$$

$$x_2 = x_c + R_c \sin \gamma_2, \tag{A5}$$

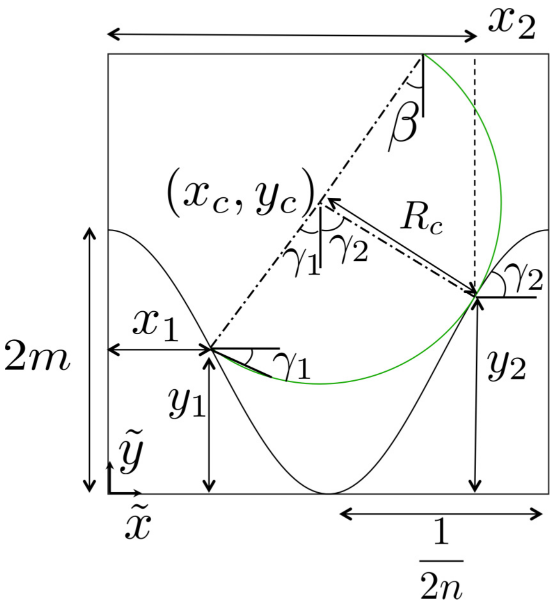

FIG. 7. Schematic of the theoretical setup. The sinusoidal geometry here is mathematically describe as $y = m[1 + \cos(2\pi n x)]$ where m and n are two dimensionless length scales given by amplitude $m = \frac{A_0}{W}$ and frequency $n = \frac{W}{\lambda}$. For low capillary and Reynolds numbers, we approximate the interface between oil and water as a circular arc that satisfies static contact angle conditions at fluid-solid interfaces. We describe the circular arc in terms of angle of intersection with horizontal at the left wall (γ_1) where $0 \leqslant x \leqslant \frac{1}{2n}$, angle of intersection with horizontal at right wall (γ_2) where $\frac{1}{2n} \leqslant x \leqslant \frac{1}{n}$, and angle of intersection with horizontal at top sidewall (β).

where

$$y_1 = f(x_1) = m[1 + \cos(2\pi n x_1)], \tag{A6}$$

$$y_2 = f(x_2) = m[1 + \cos(2\pi n x_2)], \tag{A7}$$

$$\tan\alpha = -f'(x_1) = 2\pi m n \sin(2\pi n x_1), \tag{A8}$$

$$\cos\gamma_1 = \cos\alpha\cos\theta + \sin\alpha\sin\theta, \tag{A9}$$

$$\sin\gamma_1 = \sin\alpha\cos\theta - \sin\theta\cos\alpha, \tag{A10}$$

$$\tan\gamma_2 = f'(x_2) = -2\pi m n \sin(2\pi n x_2). \tag{A11}$$

Equations (A1)–(A5) are combined with Eqs. (A6)–(A11) and are numerically solved for x_1, x_2, x_c, y_c, and R_c under the constraint $0 \leqslant y_1, y_2 \leqslant 2m$. We note that the sinusoidal pattern has only one regime where $\gamma_1 = \alpha - \theta$ is always true, unlike triangular pattern. Also, due to range of slope available in the sinusoidal pattern, the interface is always able to touch the right side of the pattern.

2. Calculation of amount of oil entrapped for triangular pattern

Once we obtain the solution for y_1, y_2, R_c, γ_1, γ_2, we can find the exact value of $\tilde{a}$ as

$$\tilde{a} = \frac{\frac{y_1 y_2}{\tan\alpha} + \frac{R_c^2}{2}[\sin(\gamma_1 + \gamma_2) - \gamma_1 - \gamma_2]}{\frac{4m^2}{\tan\alpha}}. \tag{A12}$$

Equation (A12) is consistent with Eq. (11) where we assumed the interface to be a straight line connecting y_1, y_2 and ignored the contributions due to the curvature of interface.

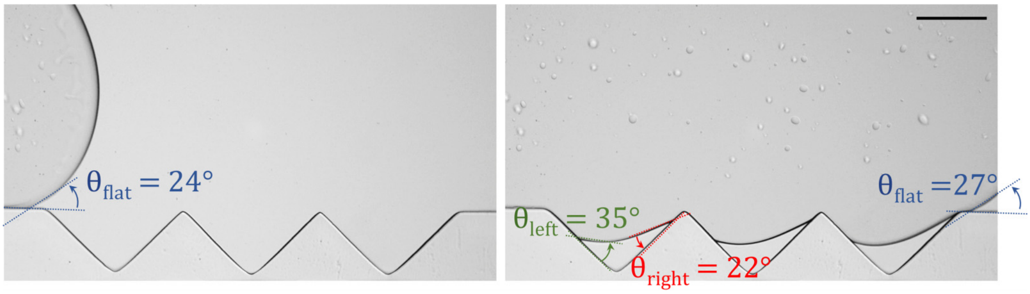

FIG. 8. Microscope images are used to evaluate the value of θ. We use $\theta = \theta_{\mathrm{flat}}$ since θ_{left} and θ_{right} are observed to be dependent on the pattern. Scale bar is 200 μm.

3. Calculation of amount of oil entrapped for sinusoidal pattern

Once we obtain the solution for x_1, x_2, y_1, y_2, R_c, γ_1, and γ_2, we can find the exact value of $\tilde{a}$ as

$$\tilde{a} = \frac{\frac{(y_1+y_2)(x_2-x_1)}{2} + \frac{R_c^2}{2}[\sin(\gamma_1+\gamma_2) - \gamma_1 - \gamma_2] - m\left[x_2 - x_1 + \frac{\sin(2\pi n x_2) - \sin(2\pi n x_1)}{2\pi n}\right]}{m/n}. \tag{A13}$$

4. Experimental measurement of contact angles

Microscope images are used to measure the contact angle of the modified sidewall (Fig. 8). We evaluate $\theta_{\mathrm{flat}} = 25^\circ$ after averaging θ_{flat} from several images. We observe that θ_{flat} is relatively constant across different patterns. In contrast, the contact angle within the triangular pattern walls θ_{left} and θ_{right} is larger than θ_{flat} due to the effect of third dimension [20,31,32]. Moreover, θ_{left} and θ_{right} are observed to be dependent on the pattern geometry, and thus we chose $\theta = \theta_{\mathrm{flat}}$. We hypothesize that differences between experiments and predictions in Fig. 5 are because the apparent contact angle within the patterned regions is different than θ. We use $\beta = 35^\circ$ for the contact angle with the unmodified wall, as evaluated in our previous work [20].

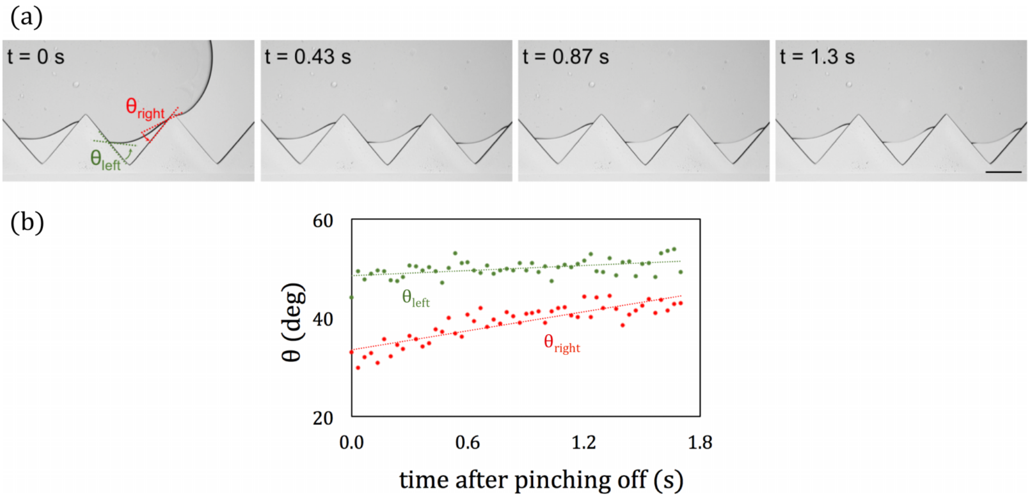

FIG. 9. (a) Microscope images of interface readjustment after pinch-off at the right side wall. (b) Time evolution of θ_{left} and θ_{right} after pinch-off. Scale bar is 200 μm.

We also analyzed the contact angle after pinch-off. We find that interface at the right side wall after pinch-off readjusts to minimize the surface energy (Fig. 9). Therefore θ_{right} increases with time whereas θ_{left} stays constant.

---

[1] N. S. K. Gunda, B. Bera, N. K. Karadimitriou, S. K. Mitra, and S. M. Hassanizadeh, Reservoir-on-a-chip (ROC): A new paradigm in reservoir engineering, Lab Chip **11**, 3785 (2011).

[2] T. W. de Haas, H. Fadaei, U. Guerrero, and D. Sinton, Steam-on-a-chip for oil recovery: The role of alkaline additives in steam assisted gravity drainage, Lab Chip **13**, 3832 (2013).

[3] C. A. Conn, K. Ma, G. J. Hirasaki, and S. L. Biswal, Visualizing oil displacement with foam in a microfluidic device with permeability contrast, Lab Chip **14**, 3968 (2014).

[4] A. Afsharpoor, K. Ma, A. Duboin, K. Mateen, S. Jouenne, P. Cordelier *et al.*, Micro-scale experiment and CFD modeling of viscoelastic polymer: Trapped oil displacement and deformation at the dead-end, in *SPE Improved Oil Recovery Symposium* (Society of Petroleum Engineers, Tulsa, Oklahoma, 2014).

[5] M. Trojer, M. L. Szulczewski, and R. Juanes, Stabilizing fluid-fluid displacements in porous media through wettability alteration, Phys. Rev. Appl. **3**, 054008 (2015).

[6] M. Jung, M. Brinkmann, R. Seemann, T. Hiller, M. Sanchez de La Lama, and S. Herminghaus, Wettability controls slow immiscible displacement through local interfacial instabilities, Phys. Rev. Fluids **1**, 074202 (2016).

[7] A. Huebner, D. Bratton, G. Whyte, M. Yang, C. Abell, F. Hollfelder *et al.*, Static microdroplet arrays: A microfluidic device for droplet trapping, incubation and release for enzymatic and cell-based assays, Lab Chip **9**, 692 (2009).

[8] P. Abbyad, R. Dangla, A. Alexandrou, and C. N. Baroud, Rails and anchors: Guiding and trapping droplet microreactors in two dimensions, Lab Chip **11**, 813 (2011).

[9] M. Sun, S. S. Bithi, and S. A. Vanapalli, Microfluidic static droplet arrays with tuneable gradients in material composition, Lab Chip **11**, 3949 (2011).

[10] M. Kang, W. Park, S. Na, S.-M. Paik, H. Lee, J. W. Park, H.-Y. Kim, and N. L. Jeon, Capillarity guided patterning of microliquids, Small **11**, 2789 (2015).

[11] H. Lee, R. L. Srinivas, A. Gupta, and P. S. Doyle, Sensitive and multiplexed on-chip microrna profiling in oil-isolated hydrogel chambers, Angew. Chem. **127**, 2507 (2015).

[12] T.-S. Wong, S. H. Kang, S. K. Y. Tang, E. J. Smythe, B. D. Hatton, A. Grinthal, and J. Aizenberg, Bioinspired self-repairing slippery surfaces with pressure-stable omniphobicity, Nature (London) **477**, 443 (2011).

[13] A. Lafuma and D. Quéré, Slippery pre-suffused surfaces, Europhys. Lett. **96**, 56001 (2011).

[14] J. D. Smith, R. Dhiman, S. Anand, E. Reza-Garduno, R. E. Cohen, G. H. McKinley, and K. K. Varanasi, Droplet mobility on lubricant-impregnated surfaces, Soft Matter **9**, 1772 (2013).

[15] A. K. Epstein, T.-S. Wong, R. A. Belisle, E. M. Boggs, and J. Aizenberg, Liquid-infused structured surfaces with exceptional anti-biofouling performance, Proc. Natl. Acad. Sci. USA **109**, 13182 (2012).

[16] J. S. Wexler, A. Grosskopf, M. Chow, Y. Fan, I. Jacobi, and H. A. Stone, Robust liquid-infused surfaces through patterned wettability, Soft Matter **11**, 5023 (2015).

[17] J. S. Wexler, I. Jacobi, and H. A. Stone, Shear-Driven Failure of Liquid-Infused Surfaces, Phys. Rev. Lett. **114**, 168301 (2015).

[18] I. Jacobi, J. S. Wexler, and H. A. Stone, Overflow cascades in liquid-infused substrates, Phys. Fluids **27**, 082101 (2015).

[19] Y. Liu, J. S. Wexler, C. Schönecker, and H. A. Stone, Effect of viscosity ratio on the shear-driven failure of liquid-infused surfaces, Phys. Rev. Fluids **1**, 074003 (2016).

[20] H. Lee, A. Gupta, T. A. Hatton, and P. S. Doyle, Creating isolated liquid compartments using photopatterned obstacles in microfluidics, Phys. Rev. Appl. **7**, 044013 (2017).

[21] S. Protiere, C. Duprat, and H. A. Stone, Wetting on two parallel fibers: Drop to column transitions, Soft Matter **9**, 271 (2013).

[22] A. Sauret, F. Boulogne, D. Cébron, E. Dressaire, and H. A. Stone, Wetting morphologies on an array of fibers of different radii, Soft Matter **11**, 4034 (2015).

[23] R. Patel and H. Benkreira, Gravure roll coating of Newtonian liquids, Chem. Eng. Sci. **46**, 751 (1991).

[24] C. Chung and S. Kumar, Emptying of viscoelastic liquids from model gravure cells, J. Non-Newtonian Fluid Mech. **221**, 1 (2015).

[25] C.-H. Huang, M. S. Carvalho, and S. Kumar, Stretching liquid bridges with moving contact lines: Comparison of liquid-transfer predictions and experiments, Soft Matter **12**, 7457 (2016).

[26] D. Dendukuri, D. C. Pregibon, J. Collins, T. A. Hatton, and P. S. Doyle, Continuous-flow lithography for high-throughput microparticle synthesis, Nat. Mater. **5**, 365 (2006).

[27] D. Dendukuri, S. S. Gu, D. C. Pregibon, T. A. Hatton, and P. S. Doyle, Stop-flow lithography in a microfluidic device, Lab Chip **7**, 818 (2007).

[28] H. Lee, S. G. Lee, and P. S. Doyle, Photopatterned oil-reservoir micromodels with tailored wetting properties, Lab Chip **15**, 3047 (2015).

[29] K. W. Bong, K. T. Bong, D. C. Pregibon, and P. S. Doyle, Hydrodynamic focusing lithography, Angew. Chem., Intl. Ed. **49**, 87 (2010).

[30] S. C. Chapin, D. C. Appleyard, D. C. Pregibon, and P. S. Doyle, Rapid micro-RNA profiling on encoded gel microparticles, Angew. Chem., Intl. Ed. **50**, 2289 (2011).

[31] W. Huang, Q. Liu, and Y. Li, Capillary filling flows inside patterned-surface microchannels, Chem. Eng. Technol. **29**, 716 (2006).

[32] M. Musterd, V. van Steijn, C. R. Kleijn, and M. T. Kreutzer, Calculating the volume of elongated bubbles and droplets in microchannels from a top view image, RSC Adv. **5**, 16042 (2015).

[33] M. Sbragaglia, A. M. Peters, C. Pirat, B. M. Borkent, R. G. H. Lammertink, M. Wessling, and D. Lohse, Spontaneous Breakdown of Superhydrophobicity, Phys. Rev. Lett. **99**, 156001 (2007).

[34] A. M. Peters, C. Pirat, M. Sbragaglia, B. M. Borkent, M. Wessling, D. Lohse, and R. G. H. Lammertink, Cassie-Baxter to Wenzel state wetting transition: Scaling of the front velocity, Eur. Phys. J. E **29**, 391 (2009).

[35] H. A. Stone, Dynamics of drop deformation and breakup in viscous fluids, Annu. Rev. Fluid Mech. **26**, 65 (1994).

[36] M. De Menech, P. Garstecki, F. Jousse, and H. A. Stone, Transition from squeezing to dripping in a microfluidic T-shaped junction, J. Fluid Mech. **595**, 141 (2008).

[37] G. C. Le Goff, J. Lee, A. Gupta, W. A. Hill, and P. S. Doyle, High-throughput contact flow lithography, Adv. Sci. **2**, 1500149 (2015).

[38] L. Cueto-Felgueroso and R. Juanes, Macroscopic Phase-Field Model of Partial Wetting: Bubbles in a Capillary Tube, Phys. Rev. Lett. **108**, 144502 (2012).

[39] L. Cueto-Felgueroso and R. Juanes, A phase-field model of two-phase Hele-Shaw flow, J. Fluid Mech. **758**, 522 (2014).